Shell engineering in soft alginate-based capsules for culturing liver tumoroids

Xuan Peng, Željko Janićijević, Sandy Lemm, Markus Laube, Jens Pietzsch, Michael Bachmann,* Larysa Baraban**

X. Peng, Ž. Janićijević, S. Lemm, M. Laube, J. Pietzsch, M. Bachmann, L. Baraban

Helmholtz-Zentrum Dresden-Rossendorf, Institute of Radiopharmaceutical Cancer Research, 01328 Dresden, Germany.
x.peng@hzdr.de
m.bachmann@hzdr.de
l.baraban@hzdr.de

X. Peng, M. Bachmann
Faculty of Medicine and University Hospital Carl Gustav Carus, Technische Universität Dresden, 01307 Dresden, Germany.

S. Lemm, J. Pietzsch
Faculty of Chemistry and Food Chemistry, School of Sciences, Technische Universität Dresden, 01307 Dresden, Germany.

M. Bachmann
Tumor Immunology, University Cancer Center (UCC), University Hospital Carl Gustav Carus Dresden, Technische Universität Dresden, 01307 Dresden, Germany.
National Center for Tumor Diseases (NCT), Dresden, Germany.
German Cancer Research Center (DKFZ), Heidelberg, Germany.
German Cancer Consortium (DKTK), Dresden, Germany.

Keywords: liver tumoroids, human hepatoma cell line (HepG2), microfluidic droplet generation system, alginate and alginate-chitosan microcapsules, permeability

Abstract

Functional interaction between cancer cells and the surrounding microenvironment is still not sufficiently understood, which motivates the tremendous interest for the development of numerous *in vitro* and *in vivo* tumor models. Diverse parameters, *e.g.*, transport of nutrients and metabolites, availability of space in the confinement, interaction with scaffolds, *etc.* make an impact on the size, shape, and metabolism of the tumoroids. Herein, we demonstrate the fluidics-based low-cost methodology to reproducibly generate the alginate and alginate-chitosan microcapsules and apply it to grow human hepatoma (HepG2) tumoroids of different dimensions and geometries. Focusing specifically on the composition and thickness of the hydrogel shell, permeability of the microcapsules is selectively tuned. The diffusion of the selected benchmark molecules through the shell has been systematically investigated using both, experiments and simulations, which is essential to ensure efficient mass transfer of small molecules and prevent large substances from reaching the encapsulated cells. Depending on available space, phenotypically different 3D cell assemblies have been observed inside the capsules, varying in the tightness of cell aggregations and their shapes. Metabolic activity of tumoroids in microcapsules was confirmed by tracking the turnover of testosterone to androstenedione with chromatography studies in a metabolic assay. Because of the high reproducibility, compartmentalization, and facile tuning of the shell thickness and permeability, our system is not only a great platform for the formation of cancer tumoroids, but also a promising tool for the design and engineering of other cells.

1. Introduction

Cancer is a major public health problem and a leading cause of death worldwide.[1] According to the estimate from American Cancer Society's Cancer Statistics Center, more than 800,000 people per year are diagnosed with liver cancer, and more than 700,000 die each year throughout the world.[1] While several types of cancer can be formed in the liver, hepatocellular carcinoma represents around 80% of all cases. Historically, *in vitro* cell lines and *in vivo* murine models are the most widely used methods for modeling liver cancers and therapy trials. Although two-dimensional (2D) culturing has enabled pioneering advances in cancer biology, it fails to recapitulate critical features of the three-dimensional (3D) organization of cells and extracellular matrix (ECM) within tissues and organs.[2, 3] Therefore, it is necessary to construct 3D structures

of cells in order to reproduce these crucial characteristics. In recent years, organoids, a tiny, 3D mass of tissue produced by the growth of stem cells (cells from which other cell types develop) have been studied as a new 3D model to resemble key features of some organs, such as gene and protein expression, metabolic function, and microscale tissue architecture in the laboratory.[4-6] Liver organoid systems derived from primary tissues or cells have been applied to investigate the mechanisms associated with liver carcinogenesis and anti-tumor therapies.[6, 7] The term 'liver organoids' usually refers to organoids representing the special sinusoidal architecture of the liver. They are ideally combined with endothelial cells, fibroblasts and Kupffer cells (sessile macrophages), while other immune cells play a subordinate role in the liver. The applications of organoids in liver tumor research (in this work referred as tumoroids) include, but are not limited to, mechanisms responsible for liver tumor initiation and progression, lineage commitment studies, drug screening and precision medicine, omics profiling, and biomarker discovery.[8-10] However, there is still limited understanding of functional interaction between liver cancer cells and the surrounding environment.[6, 7] As this environment is distinct in terms of nutrient and metabolite exchange, availability of space, interaction of cancer cells with the confining tissues, and access of the immune cells, the tumors reveal extraordinary genetic and phenotypical diversity. Thus, even with switching from 2D to 3D constructs, it is nearly impossible to mimic the variety of conditions with the help of idealized tumoroid models. It is required to develop and optimize new adaptable platforms enabling easy tuning of cell compartment parameters and thus the modification of conditions for the preparation of liver tumoroids.

Conventional highly homogeneous organoid/spheroid production methods, including extracellular matrix scaffold, spinning bioreactor, hanging drop, low-adherent cell culture plates, and magnetic levitation method, demonstrate two main challenges: 1) lack of nutrient/waste exchange and 2) lack of size reproducibility.[8, 11, 12] To overcome these disadvantages, new technological advances, such as microfluidic droplets, organ-on-a-chip, and acoustic droplet printing methods, have been introduced.[13-18] One of the most promising methods proposed is the use of microfluidic droplet systems for organoid production. With remarkable advantages including high reproducibility, miniaturization, as well as compartmentalization, these systems can produce $10^2 – 10^3$ uniform droplets within a minute, unlocking the great potential for organoid culture and overcoming the problem of low reproducibility.[19-23] Many different microdroplet generation systems have been established to generate liquid droplets, hydrogel capsules, or beads for biomedical research.[24-27]

The single-cell droplet microfluidics has enabled high-throughput single-cell sorting, genome sequencing and analysis, precise control of the microenvironment, and monitoring of the behavior of single cells in real time.[22, 28-31] Double emulsion systems within glass capillaries have been used to generate ultrathin-shell liquid/gel capsules for studying the mechanics of tumor progression and preparation of cell organoids.[32-34] Active microfluidic chips, with precise droplet size control system, have been used to investigate stem cell organoids.[35] Although there are many studies on single cells and cell organoid/spheroid preparation using microfluidic systems, deeper investigations of organoid/spheroid assembly mechanisms and their dependence on the microcontainer properties are still barely present in the literature.

Alginate (AL) based hydrogels with good biocompatibility, low toxicity, mild gelation property, and relatively low cost, have been extensively investigated and used for many biomedical applications, such as drug delivery, protein delivery, wound dressing, and cell culturing.[36, 37] Recently, with the assistance of microfluidics, monodispersed alginate hydrogel microbeads have been used to enhance 3D cell culture and examine the influence on cell toxicity by applying different gelation triggers.[38-40] However, alginate hydrogel can disintegrate in the physiological environment due to the loss of calcium ions. Because of the biological inertia and limited space within alginate hydrogels, the cells embedded in alginate cannot grow and differentiate into ordered structures or typical organoids.[41] To overcome these drawbacks, alginate capsules, alginate-based hybrid capsules, hollow microfibers, and aqueous-droplet-filled hydrogel fibers have been used for organoid engineering, cell differentiation, luminal mechanics, and drug screening, which displays the great potential of alginate shell for applications in biomedical research.[32, 34, 42-46] Diverse experimental parameters, such as concentration of chemicals, liquid viscosity, and liquid flow rate were studied in the context of capsule preparation using microfluidics.[35, 47] Studies have used molecules with different sizes to evaluate the permeabilities of alginate-chitosan and Ca-alginate/poly(ethylene imine) capsules by measuring the time that the chemicals needed to diffuse into the capsules.[35, 43] However, investigations regarding the influence of different capsule shell permeability on cell organoids are still rare. Suitable shell permeability is an essential requirement for cells within capsules to enable adequate supply of nutrients, achieve sufficient waste excretion, and prevent the entry of specific substances from reaching the loaded cells (e.g., such as immune cells and antibodies).[42] Therefore, a systematic

study regarding the impact of capsule permeability, as well as availability of free space in the container on the formation and proliferation of cell tumoroids is of high significance.

In this study, we demonstrate a microfluidics-based reproducible approach to generate alginate and alginate-chitosan-based microcapsules (AL MCs and AL-CS MCs, respectively) for culturing HepG2 liver tumoroids. In a reproducible and high-throughput manner, the system can generate hundreds of droplets within a few minutes, providing many culturing reactors in parallel and enabling robust statistical data analysis. While keeping the capsule diameter constant (*ca*. 450-500 µm), we compared the generation processes for two types of MCs by varying the thickness of the shell, from 5 to 150 µm. Permeability of AL and AL-CS MCs was also studied using several representative compounds of different sizes (from 376 Da to 2000 kDa), decorated by the fluorescent tags. Furthermore, to understand the permeation of the respective chemicals through the shell, we used a COMSOL Multiphysics model solving the system of equations governing Fickian diffusion. Finally, we demonstrate the effect of capsule permeability on the HepG2 cell aggregation, growth, and viability. The metabolic activity of tumoroids in AL and AL-CS MCs was also confirmed by tracking a substrate (testosterone) to metabolite (androstenedione) conversion with LC-MS/MS (Liquid Chromatography Tandem Mass Spectrometry). Interestingly, different geometries of cellular assemblies have been observed inside the capsules, exploiting the effects of available space, nutrient access, and interaction with the shell wall. This research provides a new point of view towards cell/organoid culturing, engineering, as well as cell proliferation in relation with the changes in capsule shell permeability.

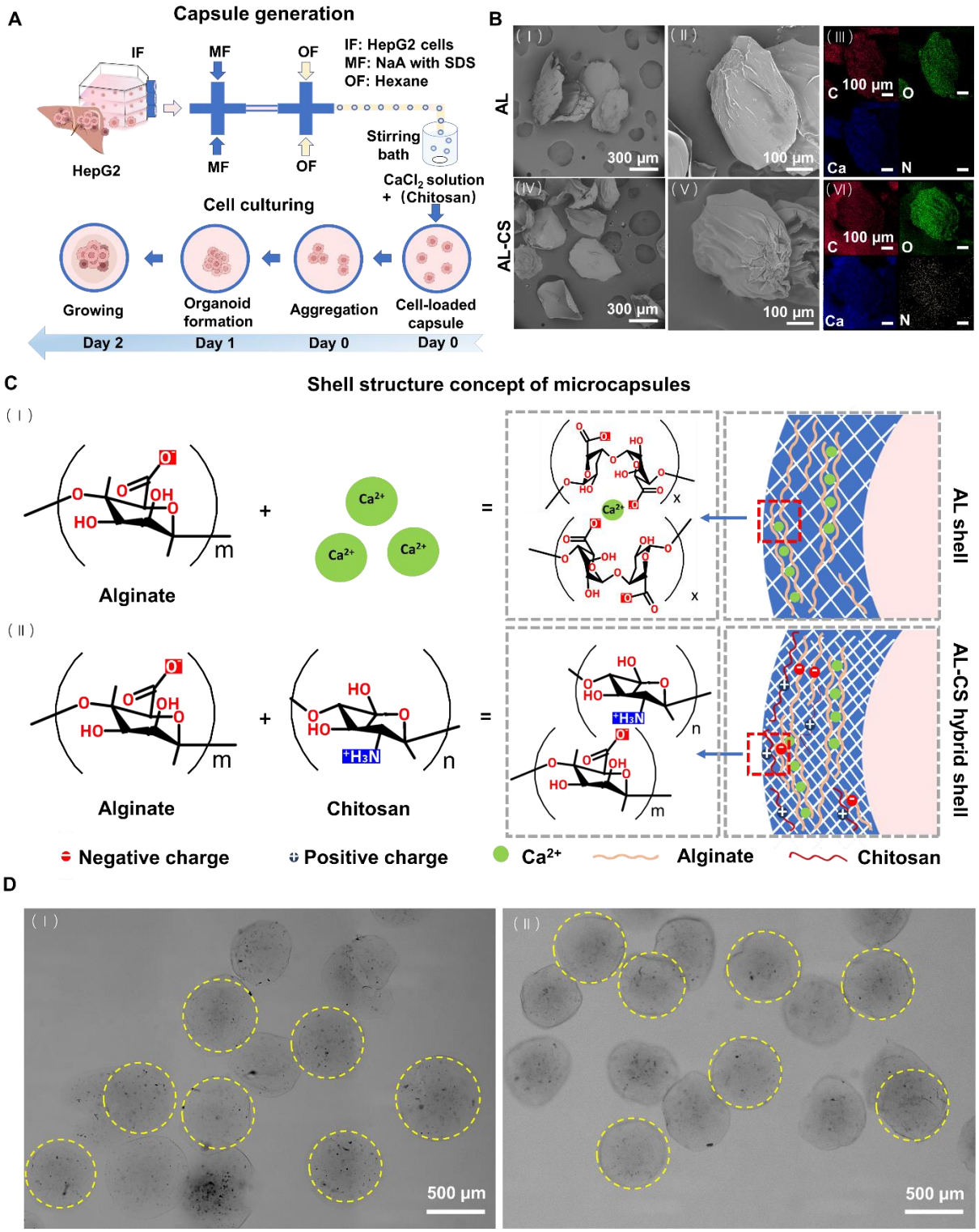

Figure 1. Microcapsule generation system and structure of microcapsules. (A) Schematic diagram of the droplet-based microfluidic system used to fabricate calcium alginate (AL) or calcium alginate-chitosan (AL-CS) composite hydrogel capsules and illustration of the timeline for main

cell tumoroid formation processes. The human hepatoma cell line (HepG2) was used in this research. (B) Representative SEM and EDS mapping images of freeze-dried AL (I-III) and AL-CS (IV-VI) microcapsules generated under the same conditions (apart from 50 mM chitosan added to the AL-CS capsule generation bath). (C) Proposed shell structure of AL and AL-CS microcapsules: formation of core-shell microcapsules through a cross-linking reaction with Ca^{2+} (I), and interaction of alginate and chitosan polymers (II) (m, n, and x designate the numbers of corresponding repeating units in polymer structures). (D) Representative optical micrographs of AL (I) and AL-CS (II) microcapsules generated under the same conditions (apart from 50 mM chitosan added to the AL-CS capsule generation bath).

2. Results and Discussion

2.1 Generation and Characterization of AL and AL-CS MCs

2.1.1 Generation of MCs

From 10^2 to 10^3 microcapsules (MCs) containing cancer cells inside the core were generated in a droplet-based microfluidic system using simple off-the-shelf components (Figure 1A and Figure S1). The microfluidic system is composed of two polytetrafluoroethylene (PTFE) cross-junctions and several pieces of tubing (PTFE, nominal inner diameter of 0.5 mm). The system comprises multiple inlets for the injection of different liquid phases used to generate the droplets (Figure S1A) and capsule fabrication units (Figure S1B&C). The multi-phase fluid inlets are utilized to infuse the inner fluid (cell culture medium, IF), middle fluid (solution of sodium alginate (NaAL) with sodium dodecyl sulfate (SDS), MF), and outer fluid (oil phase: hexane, OF) into the corresponding PTFE tubing (Figure 1A). Table S1 in Supporting Information shows the combination of the flow rates that were employed in this work to form droplets. A co-flow stream of cell medium and NaAL is formed with the assistance of SDS as the surfactant at the first cross-junction (Figure S1B). When the co-flow reaches the second cross-junction (Figure S1C), it is dispersed into small droplets with diameters ranging from ~ 400 to 600 µm in hexane. Finally, the droplets with NaAL as the outer layer gel in the $CaCl_2$ bath under soft stirring (250 rpm) and become capsules with thin shell (Figure 1B) that sediment at the bottom of the microwell. The $CaCl_2$ bath solution is

exchanged with the cell culture medium within 5 min. Encapsulated cells aggregate inside the capsules to generate tumoroids.

To determine a suitable concentration of $CaCl^2$ in the gelation bath for this study, we started with the 3% w/v solution of alginate. An optimal concentration of $CaCl^2$ in the gelation bath was experimentally determined by monitoring the microcapsule shape to be 200 mM, at which the formation of microcapsules with approximately spherical shape was observed (Figure S2, refer to section 4.4 Investigation of Parameters for Microcapsule Fabrication, for more details) which is also in accordance with previous reports[44, 48]. During the preparation of AL-CS MCs, equal concentration of $CaCl_2$ was used in the bath with the addition of chitosan (50 mM, see Supporting Information for more details). In the AL MC generation process, the droplets fall into the $CaCl_2$ solution, and an egg-box structure is formed rapidly due to the diffusion of Ca^{2+} and ionic cross-linking of alginate chains (Figure 1C(II)). The electrostatic interactions between negatively charged alginate and positively charged chitosan (Figure 1C(III)) support the formation of the hydrogel shell.

The impact of flow rate on the change of capsule dimensions was also observed. When the same flow rate parameters were used, no obvious differences in linear dimensions between AL (I) and AL-CS (II) capsules were observed under the optical microscope (Figure 1D). Therefore, AL MCs were used in further experiments to demonstrate the influence of flow rates on capsule formation. The size distributions were obtained by measuring more than 200 capsules for each combination of the flow rates (Figure S3 and Table S1). While keeping the flow rates of the IF and MF constant (total flow rate of 2.5 $mL \cdot h^{-1}$), the average diameter of MCs decreased from 530 ± 43 µm to 508 ± 56 µm with the OF flow rate increase (in the range from 10 to 20 $mL \cdot h^{-1}$). When the OF flow rate was fixed at 20 $mL \cdot h^{-1}$, the average size of MCs increased with the rise in flow rate of the IF or MF flow rates. Further, when the MF flow rate was fixed at 1.5 $mL \cdot h^{-1}$, the average MC size increased from 466 ± 41 µm to 520 ± 50 µm with the increase of IF flow rate (in the range from 0.25 to 1 $mL \cdot h^{-1}$). When the IF flow rate was kept at 1 $mL \cdot h^{-1}$, the average MC size increased from 447 ± 41 µm to 508 ± 56 µm with the increase in the MF flow rate (in the range from 1 to 2 $mL \cdot h^{-1}$). Therefore, the diameter of MCs can be efficiently tuned by changing the flow rates.

2.1.2 Characterization of MC Composition and Morphology

To investigate the impact of compositional differences between MCs on cell metabolism, we used two representative compositions, namely Ca-alginate microcapsules (AL MCs) and Ca-alginate-

chitosan microcapsules (AL-CS MCs) formed under the same flow rate conditions (see Table S1 and Figure 1C&D). For these studies, the MCs were first frozen under liquid nitrogen and freeze-dried for 36 h (refer to section 4.5 Microcapsule Characterization for more details). The samples were characterized by Fourier-transform infrared spectroscopy (FTIR) and observed using scanning electron microscopy (SEM) with energy dispersive X-ray spectroscopy (EDS) mapping. The FTIR spectra were used to compare the shell composition of AL MCs, AL-CS MCs, and pure chitosan (Figure S4). In the FTIR spectrum of AL MCs, characteristic major alginate bands were observed without notable shifts. The bands at 1592 cm^{-1} and 1414 cm^{-1} correspond to antisymmetric and symmetric stretching of CO_2^- in alginate, respectively, while the band at 1030 cm^{-1} indicates antisymmetric C-O-C stretching. This result confirms the absence of new chemical bond formation which is in accordance with the expected physical cross-linking effect arising from the interaction with Ca^{2+} ions. Recorded FTIR spectrum of pure chitosan also shows characteristic major bands such as amide I band at 1658 cm^{-1}, symmetric deformation band of CH_3 at 1375 cm^{-1}, and skeletal C-O stretching band at 1027 cm^{-1}.

FTIR spectrum of AL-CS MCs is characterized by the overlap between the alginate and chitosan bands and changes in band profiles determined by the mutual interaction of shell components. Electrostatic interactions of alginate and chitosan cause two broad bands at 1602 cm^{-1} and 1425 cm^{-1} indicating successful association of chitosan and alginate in the MC shell, probably in the form of a polyelectrolyte complex.[49, 50]

EDS mapping images show different distributions of C, O, Ca, and N in the MCs (Figure 1B). C, O, and Ca distribute evenly in both types of MCs, while N is only detected in AL-CS MCs indicating the presence of CS. Furthermore, there is also a slight difference in surface roughness between AL MCs and AL-CS MCs. By comparing the MC morphology based on SEM images in Figure S5A(II) and Figure S5B(II), we can observe that the outer surface of AL MCs (square 1) is smoother than the outer surface of AL-CS MCs (square 3). However, there is no obvious difference in the inner surface roughness of AL MCs (square 2) and AL-CS MCs (square 4).

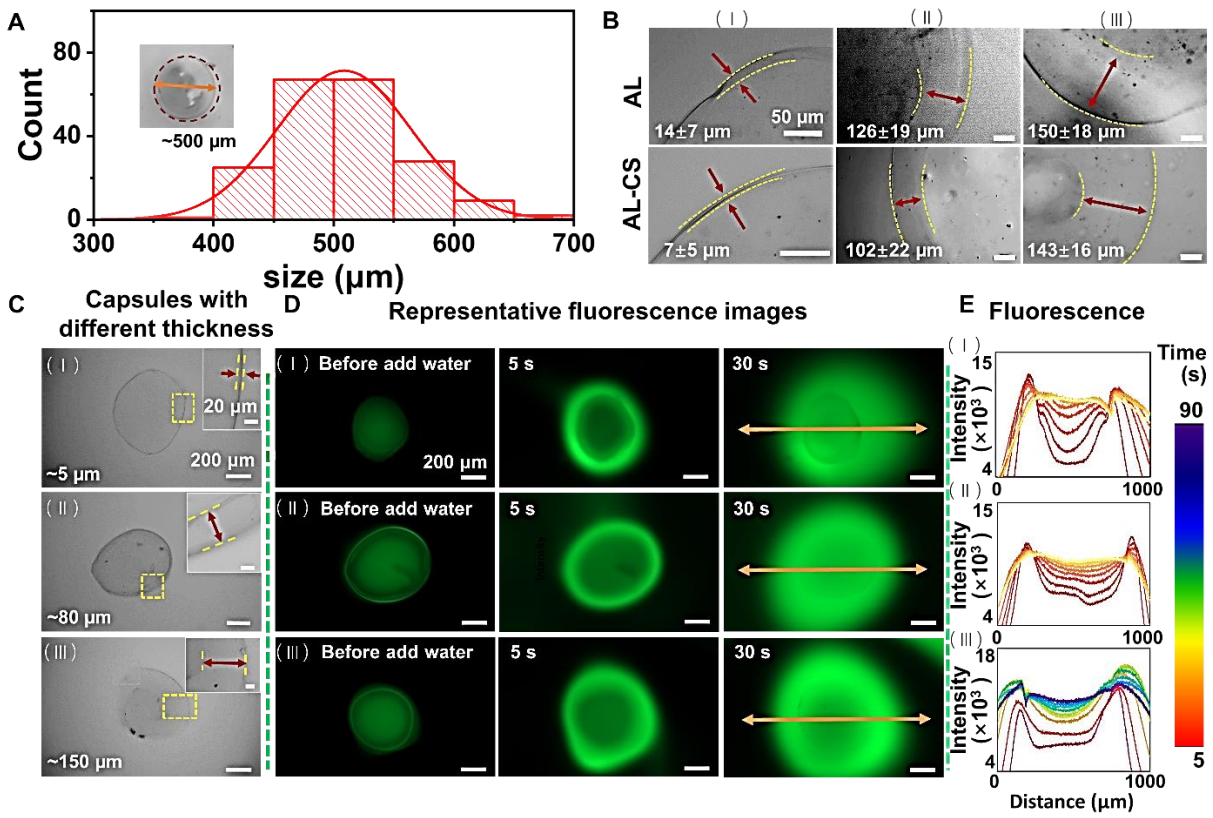

Figure 2. Relation between microcapsule permeability and shell thickness. (A) Size distribution of microcapsules (n ≥ 200 microcapsules). Flow rates of the inner, middle, and outer fluid layer are 1 mL·h^{-1}, 1.5 mL·h^{-1}, and 20 mL·h^{-1}, respectively. Inset: a representative microcapsule image. (B) Microcapsule shell thickness change with the modulation of flow rate ratio between the inner and middle fluid layers. The flow rate ratios are 1:1 (I), 1:1.5 (II), and 1:2 (III), respectively. Mean shell thickness was determined by measuring the n ≥ 50 microcapsule shells using ImageJ. Scale bars are 50 μm. (C-E) Influence of shell thickness on the permeability of microcapsules. The capsules were generated using a gelation time of 5 min. C(I), C(II), and C(III) are representative images of microcapsules with different shell thickness (~5 μm, 80 μm, and 150 μm, respectively). D(I), D(II), and D(III) are representative images of fluorescent permeability tests performed on C(I), C(II), and C(III) using fluorescein sodium (376 Da). E(I), E(II), and E(III) are fluorescence intensity profiles measured in the respective midlines of microcapsules marked with double arrow lines. Scale bars are 200 μm in the images and 20 μm in the insets.

2.1.3 Engineering of the Microcapsule Shell Thickness

To optimize the thickness of the outer shell in MCs, the OF flow rate of 20 $mL \cdot h^{-1}$ was chosen, with different flow rate ratios for IF:MF (1:1, 1:1.5, and 1:2) (for more details refer to Table S1). While these parameters enable the formation of capsules with an outer average diameter of around 500 µm (Figure 2A), change in the IF:MF flow rate ratio can significantly influence the shell thickness of the capsule. After the gelation time of 5 min, MCs with a series of different thicknesses were obtained in Ca^{2+} bath and Ca^{2+}-CS bath (Figure 2B). The thicknesses of both MC types increase with the decrease in the flow rate ratio of IF:MF, which is due to the greater alginate fractions. To quantify this effect, thicknesses of more than 50 capsules were measured for each set of experimental parameters using ImageJ. When the droplets gelled in the Ca^{2+} bath, the achieved thicknesses were 14 ± 7 µm, 126 ± 19 µm, and 150 ± 18 µm, respectively. The shell thicknesses of AL-CS MCs were only 7 ± 5 µm under IF:MF = 1:1, 102 ± 22 µm under IF:MF = 1:1.5, and 143 ± 16 µm under IF:MF = 1:15. By direct comparison of the corresponding shell thicknesses, one can observe that the shells of AL-CS MCs are thinner than those of AL MCs. The decrease in AL-CS MC shell thickness is presumably the consequence of electrostatic association between the chains of AL and CS leading to the shrinking of hydrogel structure and reduction of porosity.

2.2 Permeability of AL MCs and AL-CS MCs

Microcapsules should be able to ensure efficient mass transfer of small molecules (like nutrients and metabolites) through the shell as well as to prevent substances or biological objects of large size, such as cells and antibodies, from reaching the cells.[32, 35, 43] State-of-the-art studies were mainly dedicated to the influence of several factors on cell growth, such as concentration of alginate, gelation triggers, and gelation bath.[42, 48, 51] To understand the effect of MC shell permeability on cell and tumoroid growth, we tested the diffusion of fluorescein sodium (FSC, 376 Da) in MCs with different shell thicknesses. Representative molecules of low, moderate, and high molecular weight were used to test the size selectivity of permeation through the shell of both types of MCs (AL and AL-CS).

2.2.1 Influence of Shell Thickness

As the thicknesses of both, AL and AL-CS MCs, grow in identical manner with the increase of IF:MF flow rate ratio, we used the more stable AL-CS MCs with different shell thicknesses as representative systems to demonstrate the influence of shell thickness on microcapsule

permeability (Figure 2C). The capsules with ~5 µm, 80 µm, and 150 µm thick shell were fabricated (see Table S1 for details). At first, the capsules were immersed in a 5 mM aqueous solution of FSC for 3 min to reach a concentration equilibrium between MC interior and the outside medium. The MCs were then transferred into purified water and the diffusion was monitored using fluorescence microscopy.

There are three distinct regions (MC core, MC shell, and outside medium) defining the diffusion-controlled release kinetics of FSC absorbed by the MCs. At first, FSC diffuses out of the MC core and enters the MC shell. FSC then diffuses through the MC shell and finally becomes released into the outside aqueous medium. Figure 2D summarizes the corresponding images displaying the recorded distribution of fluorescently labeled molecules within and around the capsules. As the molecular weight of FSC is relatively low (376 Da), it rapidly permeates the shell and exits each of the MCs within *ca.* 5 s. Significantly, the fluorescence intensity in the center of the capsule with the thinnest shell (~5 µm) was lower compared to the fluorescence intensities in the second (shell thickness of 80 µm) and third capsule (shell thickness of 150 µm) after this equivalent time periods suggesting faster fluorescein sodium permeation through the thinnest shell. In this permeation monitoring experiment, fluorescent intensities for each MC were measured at different time points and the corresponding profiles were extracted from the midline profile of each MC. These fluorescence intensity profiles are depicted in Figure 2E. The average intensity in a center area (I_{in}) and the average intensity on a circle (I_{out}) was used to determine the equilibration time (Figure S6A). With the increase in thickness, the rate of fluorescence intensity change slows down (Figure S6B). For MCs with shell thickness of ~5 µm and 80 µm, the concentration equilibrium is reached within about 20 s and 50 s, respectively. However, it takes about 80 s to reach the equilibrium for MCs with shell thickness of 150 µm. In conclusion, with the shell thickness increase, the permeability of MCs decreases.

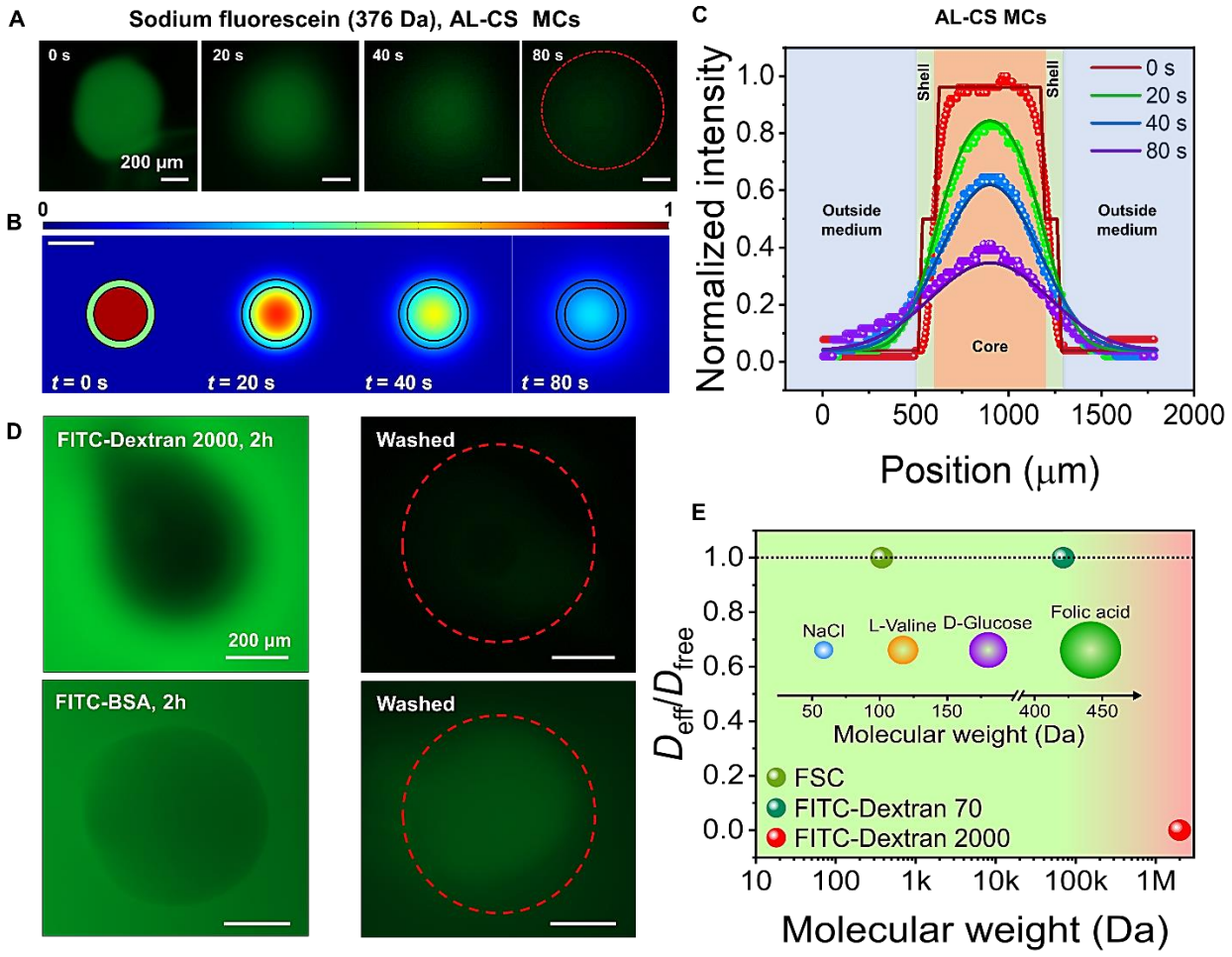

Figure 3. Permeability of AL-CS MCs generated using a gelation time of 5 min to fluorescein sodium (FSC) (376 Da), FITC-bovine serum albumin (FITC-BSA) (66.7 kDa), FITC-Dextran 70 (70 kDa), and FITC-Dextran 2000 (2000 kDa). (A) Representative images of fluorescence-based permeability tests for FSC in cell culture medium diffusing through AL-CS MCs. Scale bars are 200 μm. (B) Simulated 2D spatial profiles of FSC concentration at different time points during the release of FSC from AL-CS MCs. Scale bar is 500 μm. (C) Midline profiles of FSC release from AL-CS MCs obtained from experimental measurements of fluorescence intensity and predicted by the diffusion model. (D) Representative fluorescent micrographs obtained after immersing AL-CS MCs in FITC-BSA (1 mg·mL^{-1}) and FITC-Dextran 2000 (5 mg·mL^{-1}) solutions for 2 h before and after washing with cell medium. (E) Ratio of effective diffusion coefficient (D_{eff}) in the microcapsule shell and free diffusion coefficient in water (D_{free}) for different fluorescent reporters (FSC, FITC-Dextran 70, and FITC-Dextran 2000). FSC and FITC-Dextran 70 can freely diffuse

through the shell ($D_{eff}/D_{free} \approx 1$), while FITC-Dextran 2000 cannot permeate the shell even after a long period of immersion ($D_{eff}/D_{free} \rightarrow 0$). (E, inset) Molecular weights of representative DMEM cell culture medium components (inorganic salts, amino acids, carbohydrates, and vitamins). Due to the low molecular weight, all components of DMEM can freely diffuse through the shells of MCs.

2.2.2 Molecular Size-selective Permeability and Influence of Chitosan

AL and AL-CS MCs were generated using flow rates of IF = 1 $mL \cdot h^{-1}$, MF = 1.5 $mL \cdot h^{-1}$, OF = 20 $mL \cdot h^{-1}$ (see Table S1), which results in the average shell thickness of about 100 µm for AL and AL-CS MCs. FSC (376 Da), FITC-Dextran 70 (70 kDa), and FITC-Dextran 2000 (2000 kDa) solutions were used to represent the molecules of low, moderate, and high molecular weight, respectively, to test the size selectivity and permeability of MCs. AL MCs and AL-CS MCs were firstly immersed for predefined time periods in the solutions of fluorescein sodium (3 min), FITC-Dextran 70 (40 min), and FITC-Dextran 2000 (24 h). As both microcapsule shells show similar kinetics of diffusion for the representative chemicals, we further demonstrate the results for AL-CS MCs in the main text (AL MCs are characterized in the Supporting information, Figure S7). Furthermore, the modeling of diffusion processes was carried out using COMSOL Multiphysics.

The dynamics of fluorescence change in the MCs is summarized in Figure 3A, B&C using a representative example of FSC permeation through AL-CS MCs. Due to its low molecular weight, FSC is practically completely released from the inside of AL-CS MCs to the outside medium by passive diffusion within a couple of minutes. Such result indicates good permeability of AL-CS MCs for small molecules. To further investigate the permeability of AL-CS MCs, we exploited the diffusion model of FSC transport. We compared the simulated midline concentration profiles of FSC obtained from the diffusion model at different time points with normalized experimental data (see Figure 3C) to analyze the diffusion behavior and estimate the effective diffusion coefficient (D_{eff}) of the MC shell. Evolution of simulated concentration profiles follows the results expected from Fick´s laws indicating that diffusion rate is defined by the diffusion coefficients, MC shell thickness, and spatial gradient of solute concentration. Simulated 2D spatial profiles of FSC concentration at different time points during the permeation experiment are illustrated in Figure 3B and can be correlated with the time series of fluorescent micrographs shown in Figure 3A.

Modeling of fluorescein sodium diffusion through the AL-CS MCs was performed by assigning the diffusion coefficient corresponding to free diffusion (D_{free}) of FSC in water previously reported in the literature (D_{FSC0} = 436 $\mu m^2 \cdot s^{-1}$ [52]) as a parameter describing all regions of the geometry (MC core, MC shell, and outside medium). This reflects the reasonable initial assumption of negligible interaction between a small FSC molecule and hydrogel within the relatively thin MC shell due to the much larger mesh size of the hydrogel. Comparison between midline diffusion profiles of FSC predicted by the model and the profiles extracted from experimental data is illustrated in Figure 3C and shows a visually evident good overlap between the predicted and experimental profiles for AL-CS MCs. Therefore, we expect that FSC can diffuse freely through the MC shells immersed in cell culture medium. Practically identical results for FSC as a permeating model solute were obtained in the case of AL MCs (Figure S7) indicating that unhindered diffusion of FSC is achievable in both MC types.

Analysis of FITC-Dextran 70 diffusion yields overall similar trends comparable to the case of FSC diffusion for both MC types (Figure S8), if the literature value for diffusion coefficient of FITC-Dextran 70 in water is assigned as the parameter for all geometric regions (33 $\mu m^2 \cdot s^{-1}$ [53]). However, FITC-Dextran 70 release from MCs occurs on a much longer timescale, making the fluorescent signal more sensitive to the effects of photobleaching and quenching interactions while permeating the microcapsule shell. Therefore, the most reliable signal for real-time monitoring of FITC-Dextran 70 permeation was captured in the MC core region where experimental and predicted profiles show good overlap during the initial few minutes (Figure S8C&F). At later time points, experimental concentration profiles of FITC-Dextran 70 show an accelerating downward drift compared to the profiles predicted by the model, which can be explained by pronounced photobleaching of the fluorescent probe.

Finally, in the case of FITC-Dextran 2000 as model solute, there was no obvious fluorescence detected within the microcapsules even after they were immersed in the FITC-Dextran 2000 solution for 24 h (see Figures 3D and S9). Such result indicates that FITC-Dextran 2000 molecules cannot pass through the shell and diffuse into the aqueous core compartment of MCs.

When taking into account the hydrodynamic radii of FITC-Dextran 70 (5.8-6.4 nm[53]) and FITC-Dextran 2000 (27 nm [54]), the value of average pore size for our MC shells can be roughly estimated as 20-25 nm in cell culture medium. The estimated range of average pore size is slightly

higher than the range previously reported for 3% alginate hydrogels cross-linked with $CaCl_2$.[55] Such difference can likely be attributed to the lower cross-linking density in our hydrogels.

Our findings demonstrate that the shell pores of both AL and AL-CS MCs are large enough to allow for the transport of molecules in a broad range of molecular weights (Figure 3E) including essential nutrients (inorganic salts, amino acids, carbohydrates, and vitamins; see inset in Figure 3E), metabolites like androstenedione (286 Da), and even large macromolecules (~70 kDa), which are present in the serum.

Finally, it is necessary to associate the above permeability studies with the realistic components of the culture medium DMEM, supplemented with 10% fetal bovine serum and antibiotics, which is used for incubation of HepG2 cells. According to the findings of our microcapsule permeability experiments and diffusion modelling results, both types of microcapsules are expected to be permeable to all DMEM components. These components typically have smaller or comparable molecular weight (approximate range from 60 to 480 Da, see the inset in Figure 3E) relative to the model molecule FSC (376 Da). Thus, all DMEM components should be able to freely diffuse through the microcapsule shells. Similarly, we expect relatively unhindered diffusion to be possible for macromolecules present in the fetal bovine serum with sizes comparable to the size of FITC-Dextran 70 (hydrodynamic radius of 5.8-6.4 nm[53]).

However, molecular weight of the permeating molecules and pore size of the microcapsule shell are not the only parameters determining the diffusive transport through the microcapsule. The nature of interactions between the permeating chemical species and the shell may affect the transport of nutrients through the microcapsule. To demonstrate this, we monitored and analyzed the permeation of fluorescently labeled bovine serum albumin (FITC-BSA) through MC shells in real time. While the molecular weight of BSA is relatively small (*ca*. 67 kDa) suggesting free diffusion through the shell (see Figure 3E), its interaction with the shell may cause the misinterpretation of permeability studies carried out using fluorescent labels. For instance, while the loading tests clearly indicate the permeation of FITC-BSA through the MC shell (Figure 3D), reliable real-time monitoring of FITC-BSA diffusion was impeded by pronounced reduction in the fluorescence intensity during release experiments corresponding to the unrealistically high values of D_{eff} for FITC-BSA. This trend can be explained by electrostatic and adsorption interactions between the FITC-BSA and polyelectrolyte hydrogel matrix of the MC shell leading to significant quenching of fluorescence.

Time to equilibrium was determined by assessing the fluorescence change of FSC and FITC-Dextran 70 probes for different microcapsule types. AL and AL-CS MCs prepared using different gelation times (5 or 10 min) were firstly immersed for a predefined period in the solutions of fluorescein sodium (5 min) or FITC-Dextran 70 (60 min), and then transferred to cell medium. Equilibrium was reached after around 3 min for FSC and about 20 min for FITC-Dextran 70 in the case of AL and AL-CS MCs with shell thickness of ~100 μm which were gelled for 5 min (Figure S6C&D). Time to equilibrium for AL and AL-CS MCs with the same shell thickness gelled during 10 min (see recorded fluorescence data in Figure S10) was around 8 min in case of fluorescein sodium diffusion (around 5 min longer than for MCs gelled during 5 min). For FITC-Dextran 70, the equilibrium in these MCs was not reached even after 60 min of immersion and the initial fluorescence intensity in both, AL and AL-CS MCs, was significantly lower than the fluorescence intensity in MCs prepared using the gelation time of 5 min. Such trend in the findings indicates that the increased gelation time leads to the decrease in capsule permeability, presumably due to the more effective cross-linking. Comparison of fluorescence intensities recorded for the two MC types shows that the initial fluorescence intensity of each probe in AL-CS MCs was much lower than the intensity in AL MCs.

Through these assessments, we confirmed the presence of different selective shell permeabilities for AL MCs and AL-CS MCs ensuring the desired physical isolation of the encapsulated tumoroids from the large biochemical or biological components. In addition, gelation time and the thickness of the MC shell can be used as key parameters to actively modulate the rate of nutrient diffusion into the MCs. Furthermore, investigation of the size-selective permeability suggests that the appropriate transport of critical nutrients for maintaining cell viability and function such as glucose, amino acids, and metabolites (e.g., androstenedione and 6-hydroxytestosterone) can be successfully engineered by optimizing the aforementioned key parameters. AL MCs and AL-CS MCs generated in this study meet the criteria for cell encapsulation and represent a promising platform for investigating the influence of various chemical agents on the growth and viability of cells and tumoroids.

2.3 Growth and Metabolism of HepG2-Derived Tumoroids in AL MCs and AL-CS MCs

Results of our MC permeability assessment show that, although the properties of AL and AL-CS MCs are similar, AL MCs still exhibit more efficient mass transfer during the same time period

than AL-CS MCs generated under the same conditions (Figure S11). Next, we investigated the variations in cell proliferation using HepG2 liver cancer cells (a common *in vitro* model system for the study of polarized human hepatocytes[56]) as the model system growing within AL MCs and AL-CS MCs which are characterized by different permeability and shell properties.

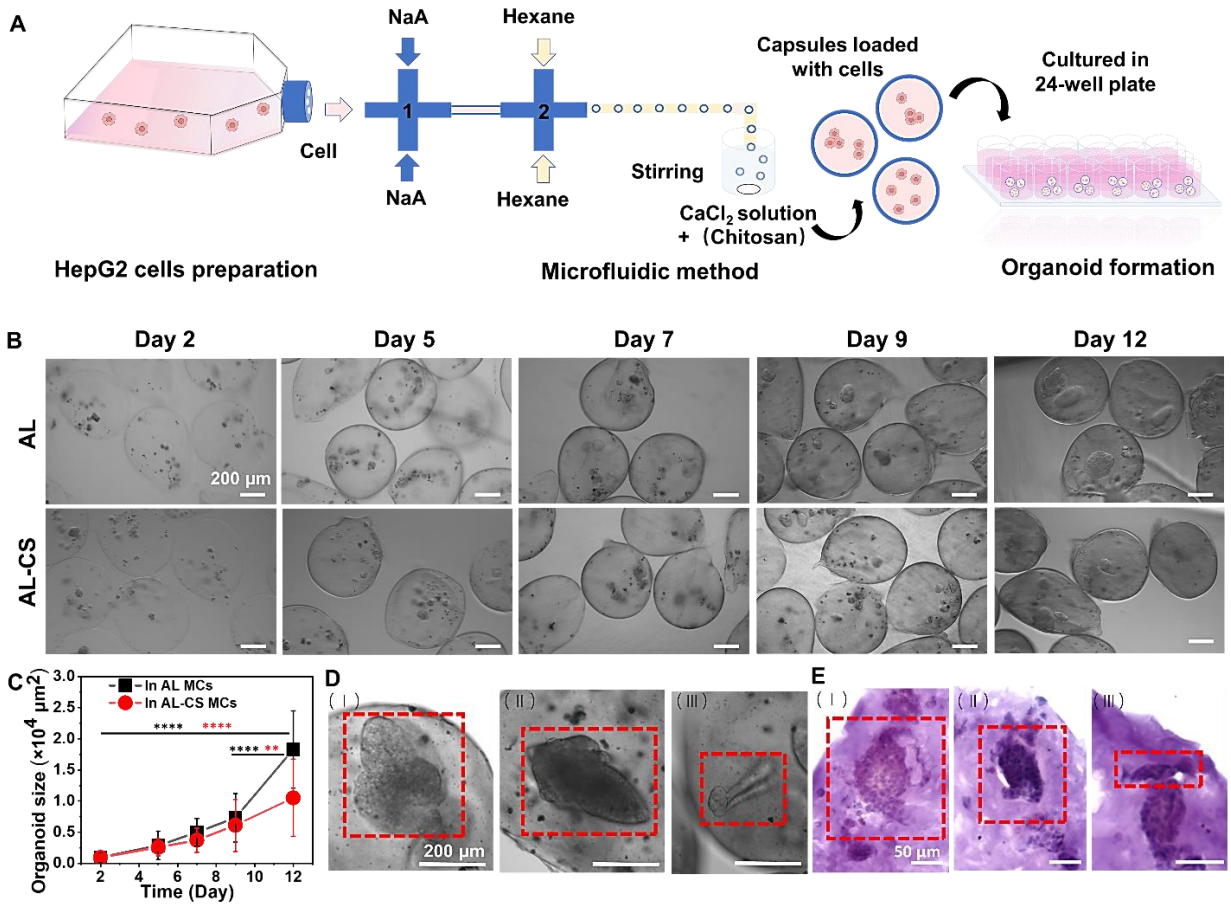

Figure 4. Rapid formation of liver tumoroids. (A) Illustration of preparation processes of the liver tumoroids using HepG2 cells. (B) Representative optical images of AL and AL-CS microcapsules loaded with liver tumoroids on day 2, day 5, day 7, day 9, and day 12. (C) Tumoroid size measurement in AL and AL-CS MCs (data shown as mean ± SD; One-way ANOVA test; **$p < 0.01$ and ****$p < 0.0001$, $n \geq 10$). (D) Different cell gathering in microcapsules: loose clusters (I), tight clusters (II), and tadpole clusters (III). (E) H&E staining of different cell clusters in microcapsules: loose clusters (I), tight clusters (II), and tadpole clusters (III). The scale bars in (B & D) are 200 μm, and in (E) are 50 μm.

2.3.1 Encapsulation, Cultivation and Characterization of HepG2-Derived Tumoroids in AL MCs and AL-CS MCs

We investigated the feasibility of using AL MCs and AL-CS MCs as 3D scaffolds for engineering liver tumoroids from inoculated HepG2 cells (Figure 4A). Prior to the formation of such tumoroids, HepG2 cells were first cultured in a flask, until their initial viability was higher than 85%. After subsequent trypsinization and resuspension, culture medium with cell density of 1×10^7 cells·mL^{-1} was used as the IF for encapsulation experiments at a flow rate of 1 mL·h^{-1}. This protocol resulted in an optimized concentration of approx. 250 cells per MC. A 3% w/v alginate solution with 0.5 mM SDS was used as middle fluid (MF) at a flow rate of 1.5 mL·h^{-1}. The droplet generation process was followed by 5 min of gelation in a solution containing 200 mM Ca^{2+} with or without added chitosan (50 mM), which resulted in the shell thicknesses of 126 ± 19 µm (AL MCs, n = 50) and 102 ± 22 µm (AL-CS MCs, n = 50) (for details refer to section 2.1.3 Engineering of the Microcapsule Shell Thickness). Afterwards, the capsules were collected in a 24-well microplate, washed twice with the cell culture medium and cultured in the microplate wells under a humidified atmosphere with 5% CO_2 at 37 °C. After one day of culturing within the MCs, the cells gather into clusters and then form the seeds for larger tumoroids. Within one week, an average size of *ca.* 5000 µm^2 within both, AL MCs and AL-CS MCs was reached, as demonstrated in Figure 4B. In the following 5 days, the tumoroids in AL MCs maintained the rapid growth rate, while those in AL-CS MCs exhibited slower proliferation.

To quantitatively evaluate the increase in the dimensions of these liver tumoroids in MCs, the average sizes of the tumoroids were calculated by measuring more than 50 tumoroids (Figure 4C) in separate confinements. A trend can be observed showing that tumoroids grow faster in AL MCs compared to AL-CS MCs during 12 days of culturing. Tumoroids in AL MCs increase in size on average from ~900 µm^2 to ~20,000 µm^2, while the average size of tumoroids in AL-CS MCs reaches only ~10,000 µm^2 on day 12.

Notably, we observed that cells gather differently during the first 5 days of proliferation. Most of the cells gathered as loose clusters (LC, Figure 4D(I)) showing a high degree of transparency and weak attachment of cells to each other. Some categories of cells were organized into tight clusters (TiC, Figure 4D(II)), where the intercellular distance was decreased as indicated by low transparency in comparison with LC. Interestingly, we also observe the elongated clusters (resembling the tadpole shape) that have their origin at the surface of the shell and point towards

the capsule center in both AL MCs and AL-CS MCs (TaC, Figure 4D (III)). We assume that such rare type of cancer cell assembly was formed due to the local surface inhomogeneities at the inner side of the MC shell (including the effect of electrostatic interactions) facilitating the anchoring of the cells. Abundance of nutrients near the MC surface enables cell division along the radial direction and thereby determines the final outwards pointing orientation of the tadpole clusters. To compare the aggregation levels of these clusters, the MCs were embedded in gelatin and cut into 20 μm thick slices for hematoxylin and eosin (H&E) staining (Figure 4E). It is obvious that the LCs show the lowest contrast, followed by a higher contrast of TaCs, and the TiCs show the highest contrast. The results of H&E staining experiments confirm that cells within the MCs gather into clusters of different tightness.

To assess the differences in tumoroid formation between the two types of MCs, more than a hundred tumoroids were counted on day 9 and classified based on clustering morphology. The fractions of LCs, TiCs, and TaCs in more permeable AL MCs were 62.6%, 25.8%, and 11.6%, while the fractions of same clusters in less permeable AL-CS MCs were 39.6%, 49.5%, and 10.9%, respectively. Such results indicate that HepG2 cells gather into tighter clusters within capsules exhibiting lower permeability. Hence, different permeability of MCs does not only influence the size and viability of liver tumoroids, but also their formation. Therefore, by tuning the permeability of MCs for liver cancer cell culturing, we can engineer tumoroids suitable for biomedical research applications such as drug testing and metabolism assessment.

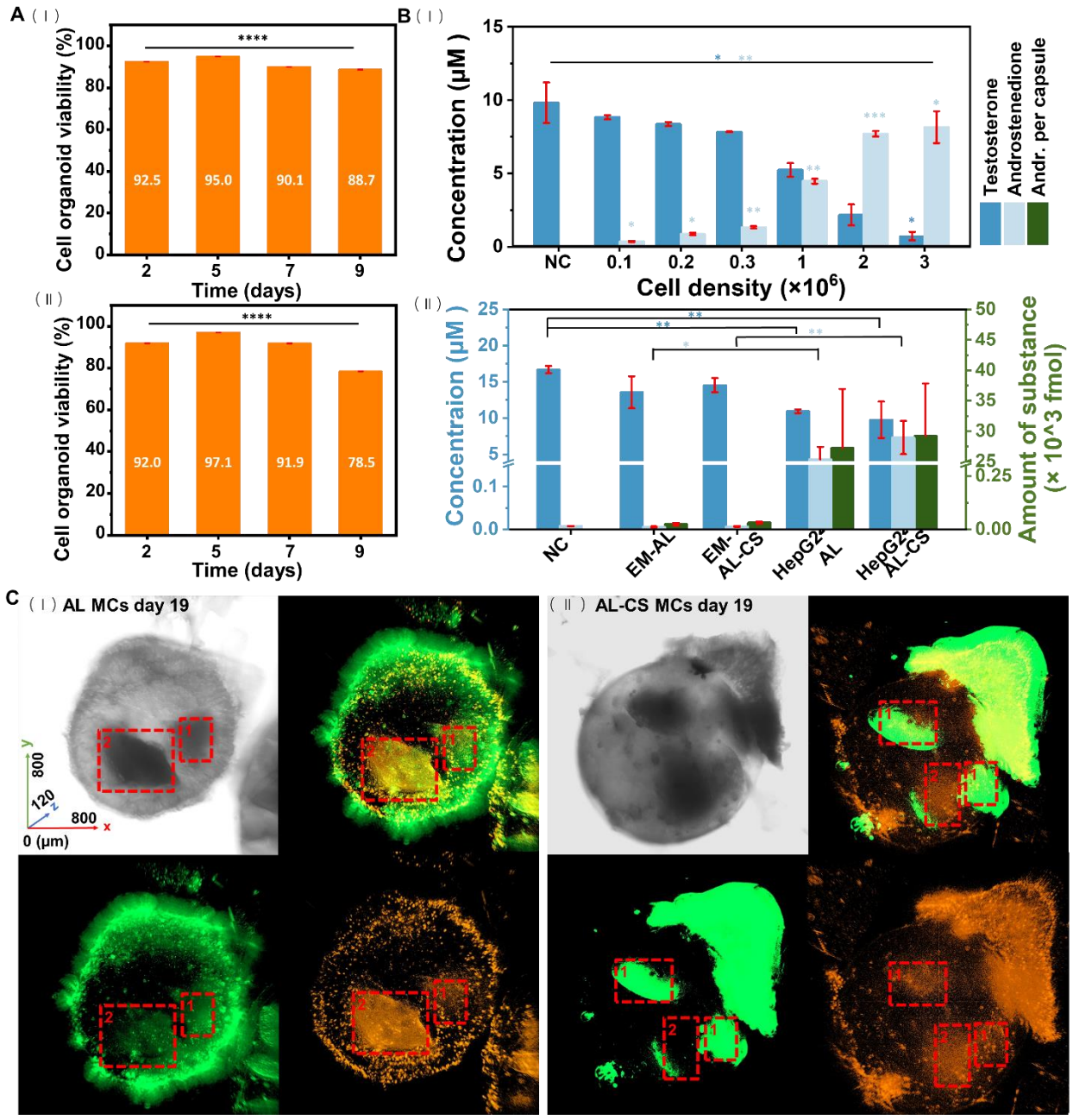

Figure 5. Cell tumoroid viability and metabolic activity. (A) Viability of tumoroids in AL (I) and AL-CS (II) microcapsules during culturing at day 0, day 2, day 5, day 8, and day 12 using Calcein AM/PI (Live/Dead) assay. (B) Concentrations of testosterone and androstenedione in HepG2 monolayer (I) and in encapsulated HepG2 tumoroids (II) after a 4 h of incubation with 10 μM testosterone. Upper panel illustrates metabolic data for the monolayer and highlights the influence of different cell densities on the metabolic activity. Lower panel shows metabolic data for encapsulated tumoroids and respective controls. Data shown as mean ± SD; One-way ANOVA

test for (A and B(I)), Student's t-test for (B); *p < 0.05, **p < 0.01, ***p < 0.001, ****p < 0.0001, n≥3. Notation: NC = no cells, EM = empty capsules, AL = alginate, AL-CS = alginate-chitosan, Andr. = androstenedione. (C) Representative 3D optical images and Live/Dead staining images of cell-loaded AL microcapsules (I) and AL-CS microcapsules (II) on day 19: regions marked with 1 designate loose clusters and those marked with 2 designate tight clusters.

2.3.2 Tumoroid Viability and Metabolism

To measure the overall viability of liver tumoroids in different MCs, Calcein AM/PI (Live/Dead) staining was used. We confirmed that after one week of culturing, the viability of tumoroids was higher than 90% in AL MCs and higher than 80% in AL-CS MCs (Figure 5A). Our data also shows that the viability of liver tumoroids in AL MCs remains higher than 80% on day 12, while the viability of liver tumoroids drops slightly below 80% in AL-CS MCs. The tumoroid viabilities in three different cluster categories were also compared using Live/Dead staining on day 9. The viabilities of LCs and TaCs were both higher than 90%, while the viability of TiCs was only 65% (Figure S12). The greater proportion of dead cells in TiCs is presumably due to hypotonicity caused by tight packing of cells.

We continued the culturing of tumoroids in the MCs also for a longer period. Interestingly, compared to the previous report of capsules with a thin shell becoming deformed and ruptured within 8 to 12 days,[44] the TaCs in our capsules drilled through the MC shell and proliferated outside of MCs within 14 to 20 days (Figure S13). The 3D images of AL MCs and AL-CS MCs showing a clear structural difference in HepG2 cell growth on two different MC types were also obtained (Figure 5C). For comparison purposes, we also collected the 3D Live/Dead staining data. The cells tend to almost cover the outer surface of AL MCs evenly, while they are prone to proliferate vertically on the outer surface of AL-CS MCs, thereby forming a pyramid-like structure. In both types of MCs, there is a higher proportion of dead cells within the MC core, which is presumably caused by stronger effect of hypotonicity and limited nutrient access in this region. However, the cells proliferating on the surface of microcapsules are still alive even after one month (Figure S14).

To confirm the metabolic ability of the cancer tumoroids, testosterone to androstenedione turnover was chosen as suitable parameter and measured with LC-MS/MS (liquid chromatography tandem mass spectrometry, Figure 5B)[57]. As expected for viable HepG2 cells, both HepG2 cultured in

AL MCs or AL-CS MCs showed marked consumption of testosterone accompanied with an accordingly high formation of androstenedione and hence overall high metabolic ability of the cells. Interestingly, the detected concentration of androstenedione in AL-CS MCs was found to be slightly higher than in AL MCs (Figure 5B(II)). This result can be mainly attributed to the breaking of many AL MCs during the KHB washing process, which led to the removal of some tumoroids and broken capsules from the wells. By comparing with the metabolic results for different cell densities (Figure 5B(I)), it was found that the formed amount of androstenedione in AL-CS MCs approximately corresponds to the amount formed by 1-2×10^6 cells·$well^{-1}$. To be more accurate when assessing the metabolic ability of HepG2 cells in two MC types, the remaining number of MCs of each type was determined after incubation and the corresponding average concentration of androstenedione per capsule was calculated. Obtained results (Figure5B(II)) show similar average concentrations of the metabolite generated by cells in AL MCs and AL-CS MCs. These results are in accordance with other experimental data generated in this study, confirming that HepG2 cells can not only adequately proliferate but also retain their metabolic ability in either AL MCs or AL-CS MCs. We also did a quick exemplary calculation and found that approx. 2.23 fmol androstenedione is formed by 1 cell in monolayer within the 4 h incubation based on cell growth (data calculated from Figure 5B(I), 1×10^4 cells). Based on initial cell density and their proliferation rate (approx. 1.6×10^4 cells after culturing 7 days), as well as the measured androstenedione amounts (2.82×10^4 fmol/capsule) in the capsules, there is approx. 1.76 fmol androstenedione formed by 1 cell in tumoroids within the 4 h incubation. This result indicates that the encapsulated cell shows a comparable manner to monolayer cells. The slight deviation maybe caused due to the different conditions of culturing, including 3D structure of tumoroids, matrix of capsules, and prolonged incubation. Promising proliferation and metabolic capabilities enable their use as liver tumoroids models for further research in biology and medicine.

In addition, the method exemplarily was also extended to the human melanoma cell line A375, a cell line that can exhibit anti-xenobiotic activity by inducing various cytochromes.[58] Which showed clear, albeit lower metabolic activities than HepG2 cells (Figure S15). The melanoma cells differ from the HepG2 cells in terms of proliferation, metabolic capacity and malignancy, among other things, which should serve as evidence at this point that the methodological approach investigated here can in principle also be applied to other tumor entities.

3. Conclusion

In summary, a low-cost cross-junction based microfluidic droplet system was constructed and used to generate AL MCs and AL-CS MCs for culturing liver HepG2 tumoroids growing in supplemented DMEM medium. This system can generate $10^2 – 10^3$ MCs within a few minutes and hence provide many reproducible culturing reactors in parallel for research. We systematically investigated the effects of capsule generation parameters and shell thickness (range from ~ 5 μm to 150 μm) on capsule permeability. Suitable permeability of both microcapsule types was confirmed using fluorescent probes of different sizes, and it represents an important asset for the growth of cancer cells inside microcapsules allowing sufficient nutrient supply and preventing the entry of large contaminants from the outside medium. The AL-CS MCs show lower permeability than AL MCs generated under the same experimental conditions. Moreover, a numerical model in COMSOL Multiphysics was used to simulate and analyze the kinetics of the MC diffusion process. Results of the modeling match the diffusion kinetics observed in the experiments and provide the possibility to estimate the effective diffusion coefficient of the MC shell. In the early stage of tumoroid culturing (*ca.* one week) higher viability of cells was observed in less permeable AL-CS MCs than in AL MCs fabricated under the same conditions, while this viability trend becomes reversed in the later culturing stage. Such cell viability alterations in AL-CS MCs are presumably caused by the lower permeability and hypotonicity which aid cell aggregation in the early stage but simultaneously also enable slower nutrient exchange for cell proliferation in the later stages. Furthermore, we observed different loose and tight cell cluster morphologies, also including cell proliferation along radial directions in both MC types. The tumoroids in AL MCs and AL-CS MCs both show a comparable manner to gold standard methods like monolayer assays. Compared to the previously reported cell organoid preparations using microfluidic systems, our system can produce MCs with tunable permeability, hence providing a great platform for the formation of liver tumoroids. Since the permeability differences between MCs influence tumoroid formation, cell proliferation, and metabolic ability of cells, engineering of MC permeability is an effective method for the design of liver tumoroids. Our approach holds promise for the design and culturing of various tumoroids and opens a new perspective towards organoid engineering.

4. Experimental/Methods Section

4.1 Materials

In this study, we utilized the following reagents: sodium alginate (NaAL, Sigma-Aldrich, N/A), sodium dodecyl sulfate (SDS, Sigma-Aldrich, 98.5%), chitosan (CS, Sigma-Aldrich, low molecular weight, N/A), phosphate Buffered Saline tablet (PBS, Sigma-Aldrich), $CaCl_2$ (Merck, 99.5%), hexane (Fisher Scientific, 95%), fluorescein sodium (FSC, Sigma-Aldrich, 376.27 Da), Albumin–fluorescein isothiocyanate conjugate (FITC-BSA, Sigma-Aldrich, 67 kDa), Fluorescein isothiocyanate–dextran (FITC-Dextran 70, Sigma-Aldrich, 70 kDa), FITC-Dextran sulfate sodium salt (FITC-Dextran 2000, Sigma-Aldrich, 2000 kDa), acetic acid (Carl Roth, 100%), acetone (Sigma-Aldrich, 96%), acetonitrile (ACN, Fisher Scientific, 99.9%), Trypsin (Biochrom), sucrose (Carl Roth), gelatin (Carl Roth), Calcein AM and Propidium iodide (PI) (VWR (Corning)), Hematoxylin (Sigma-Aldrich), Eosin B (Sigma-Aldrich), RotiMount (Carl Roth), Roticlear (Carl Roth), testosterone (Sigma-Aldrich). The HEPES-supplemented Krebs-Henseleit-Buffer (pH 7.4, KHB) was freshly prepared using HEPES (5.95 g/L), D-glucose (2.0 g/L), magnesium sulfate (0.141 g/L), potassium dihydrogenphosphate (0.16 g/L), potassium chloride (0.35 g/L), sodium chloride (6.9 g/L), calcium chloride dihydrate (0.373 g/L), and sodium bicarbonate (2.1 g/L) followed by adjustment to pH 7.4 with NaOH. All reagents were used as received without additional purification.

4.2 Solution Preparation

The middle fluid (MF) was prepared by dissolving NaAL in deionized water to reach the concentration of 3% w/v and then adding SDS to reach 0.5 mM concentration.

The outer fluid (OF) solution was prepared by dissolving CS in deionized water to reach the concentration of 1% (w/v) and then adjusting the pH to 5 using acetic acid.

The $CaCl_2$ bath was prepared as an aqueous solution of $CaCl_2$ with concentrations in the range from 100 mM to 400 mM. The $CaCl_2$ bath with CS was prepared by adding 25 µL of 1% (w/v) CS solution into $CaCl_2$ bath to reach 1000 µL of solution volume.

NaAL solution was sterilized under UV light for 2 h. Other solutions were purified using 0.2 µm syringe filter (VWR). All prepared solutions were stored in the refrigerator at 5 °C until further use.

4.3 Formation of the Microcapsules

For preparation of alginate microcapsules (AL MCs) or alginate-chitosan microcapsules (AL-CS MCs), water/water droplets were generated using cross-junctions water-in-oil system. Briefly, the three fluid phases (cell medium: IF, MF, OF) were loaded into 1 mL, 2.5 mL, and 10 mL syringes (SGE, Analytical science). Flow rates used in this work are shown in Table S1. The flow rates used in the generation of MCs for cell culturing were: q_{IF} = 1 mL·h^{-1}, q_{MF} = 1.5 mL·h^{-1}, q_{OF} = 20 mL·h^{-1}. After the initiation and stabilization of the flows, compound capsules were directed to a gelation bath which contained 200 mM $CaCl_2$ (and 50 mM CS when preparing AL-CS MCs). The concentration of $CaCl_2$ and CS was determined according to the cell culturing test to reach a suitable permeability for cell proliferation (refer to Supporting Information for more details).

4.4 Investigation of Parameters for Microcapsule Fabrication

To produce MCs with a uniform size and morphology in a controllable fashion, we explored the effects of some key parameters in the capsule generation system. To investigate the influence of flow rates in the microfluidic system, we examined the inner fluid (IF) flow rate ranges from 0.5 to 1 mL·h^{-1}, middle fluid (MF) flow rate ranges from 0.5 to 2 mL·h^{-1}, and the outer fluid (OF) flow rate ranges from 10 to 20 mL·h^{-1}. The exact flow rates are listed in Table S1. An optical microscope (Axio Observer, Zeiss) was used to capture the images. These acquired images were later used to manually measure the sizes of MCs using ImageJ.

To investigate the effect of $CaCl_2$ concentration on cross-linking, different concentrations of $CaCl_2$ in the gelation bath (100, 200, 300, and 400 mM) were used to fabricate the MCs.

4.5 Microcapsule Characterization

Fourier-transform infrared spectroscopy (*FTIR*): Fourier transform infrared spectroscopy (FTIR) was performed on a Spectrum 100 (Perkin Elmer, Inc., USA) spectrometer with a scan range of 4000-400 cm^{-1}. To assess the chemical composition of AL MCs and AL-CS MCs, FTIR spectra of AL MCs, AL-CS MCs and CS were obtained from freeze-dried capsules using Tensor II (Bruker) equipped with an attenuated total reflectance (ATR) accessory at ambient temperature with a wavenumber resolution of 1.5 cm^{-1}.

The MC samples dispersed in aqueous solution were first frozen under liquid nitrogen for 5 min, and then freeze-dried (Alpha 2-4 LSC plus, Christ) for 36 h.

Scanning electron microscopy (*SEM*)**:** To observe the morphology of MC surfaces, freeze-dried capsules were fixed on a conductive carbon adhesive tape. The SEM images of MC cross section were acquired using the Phoenix XL Microscope at an acceleration voltage of 5 kV after sputter-coating an approximately 7 nm thick layer of gold. EDS mapping and electronic elemental analysis were recorded using an SEM detection accessory at an acceleration voltage of 15 kV.

4.6 Immunoisolation and Diffusion Experiments

The diffusion through the shell of hybrid MCs was monitored using 5 mM solution of FSC (376 Da), 1 mg·mL^{-1} solution of FITC-Dextran 70 (70 kDa), and 5 mg·mL^{-1} solution of FITC-Dextran 2000 (2000 kDa), as fluorescent probes representing small molecules, proteins, and macromolecules, respectively.

Fluorescent probe immersion and permeation experiments: The newly fabricated MCs were immersed in the solution of the corresponding fluorescent probe that is expected to diffuse across the MC shell and enter the MC after a predefined period in the dark at ambient temperature (3 min for fluorescein sodium and 30-60 min for FITC-Dextran 70). The MCs containing absorbed fluorescent probe were subsequently immersed in water or cell medium and the diffusion was monitored under an optical microscope (Axio Observer, Zeiss). The light detection mode contained a filter set (495 nm beamsplitter, 450-490 nm excitation, and 500-550 nm emission, Zeiss). Fluorescent micrographs were acquired as snapshots at different stages of the diffusion process at defined time points considering the permeability of different fluorescent probes. To test the influence of thickness change on permeability, fluorescein sodium experiment was carried out in water and lasted only 2 min in total (with the exposure time of 0.2-0.3 ms for each micrograph). To compare the permeability of AL MCs and AL-CS MCs in cell medium, experiment with fluorescein sodium lasted 3-10 min (with the exposure time of 0.2-0.3 ms for each micrograph), experiment with FITC-BSA (1 mg·mL^{-1}) lasted 30-120 min (with the exposure time of 5-10 ms for each micrograph), while the experiment with FITC-Dextran 70 and 2000 continued for 30-120 min in total (with the exposure time of 0.5-2 ms for each micrograph). In the case of FITC-Dextran 2000 probe, the micrographs were acquired after 24 h (with the exposure time of 10-20 ms). The absolute fluorescence intensity was measured using ZEN 3.3 (blue edition) software.

4.7 Modeling of solute diffusion through AL and AL-CS MCs

4.7.1 Preprocessing of fluorescent micrographs for solute diffusion modeling

Fluorescence images were acquired at predefined time points determined by preliminary tests of diffusion rate using the optical microscope (Axio Observer, Zeiss). In order to extract required data for monitoring the diffusion of solutes through MCs, raw fluorescence micrographs were processed using ImageJ (1.53k[59]) and then imported in MATLAB programming package (Release 2018b, The MathWorks, Inc., Natick, Massachusetts, United States) to extract the MC midline fluorescence intensity profiles using a custom script.

To measure the effective radius, MCs were segmented from the green channel of fluorescence images recorded at $t = 0$ using automatic thresholding and the ellipse was fited to the outline of the segmented MC object. Effective MC radius was calculated as $r = (a+b)/2$ where a and b are the semi-major and semi-minor axes of the fitted ellipse. Mean thickness of the microcapsule shell was determined directly from the green channel of fluorescence micrographs acquired at $t = 0$ (before bringing MCs in contact with the release medium) by manually measuring the thickness at 20 random locations on the shell and then calculating the mean value. To achieve accurate spatial alignment of diffusion profiles within a time series of fluorescence recordings, raw fluorescence micrographs at each time point were subjected to threshold-based segmentation applied on the green channel. Afterwards, MC ''center of mass'' coordinates were measured in ImageJ for each of the segmented MC objects. Data about microcapsule position were further used as an input to the custom MATLAB script to align extracted midline fluorescence intensity profiles. All profiles were normalized (range from 0 to 1) and further used to define initial conditions in the model or to compare modeling results with the experimental data.

4.7.1 Modeling of solute diffusion through AL and AL-CS MCs

Modeling of diffusion through microcapsules was performed in COMSOL Multiphysics (COMSOL Multiphysics® v. 5.2, COMSOL AB, Stockholm, Sweden) using the Chemical Species Transport module and Transport of Diluted Species interface applied to the 2D circular geometry of the model to minimize the computation time, while assuming axial symmetry around the *z*-axis to adhere with spherical symmetry of the MCs. The model takes into account the diffusion of a single fluorescent compound (fluorescein sodium or FITC-Dextran 70) as a dilute solute in aqueous media through three different regions of interest represented as a semicircle (MC core)

and two consecutive semicircular rings (MC shell and outside medium) (Figure S16). Geometry of the analyzed capsule was represented using the mean values of the MC core radius and shell thickness obtained from the previously described image analysis in ImageJ. Outside medium is represented as an additional outer shell added after the microcapsule shell with the thickness calculated to reach 2.5 mm radius of the outermost sphere defining the boundary of the release medium.

To simulate Fickian diffusion of the solute within the model geometry, we numerically solve the system of equations describing Fick´s laws built into the Transport of Diluted Species interface[60]:

$$\phi = -D\nabla C \tag{1}$$

$$\frac{\partial C}{\partial t} = D\nabla^2 C \tag{2}$$

where ϕ designates the molar flux, D the diffusion coefficient, and C the molar concentration of the solute.

Simulation of the diffusion process was performed under the following assumptions:

1) Concentration of the solute is directly proportional to the fluorescence intensity.
2) Diffusion of the solute obeys Fick´s laws, takes place through homogeneous materials where each region can be represented with an effective mean diffusion coefficient, and there are no additional transport mechanisms involved in the process.
3) Solute diffuses freely in the aqueous solution within the microcapsule core and the outside medium with an equal mean diffusion coefficient.
4) There is no solute flux through the outermost spherical boundary of the outside medium.

Initial concentration profile of the solute was defined using average values from the experimental midline profiles corresponding to the fluorescence micrographs acquired at a first time point after bringing MCs in contact with the release medium. Initial concentration values were extracted from the midline profiles of fluorescence intensity in such manner that each average corresponds to a distinct region of the microcapsule geometry (MC core, MC shell, and outside medium).

Concentration profile of the fluorescent solute was calculated for the entire geometry in time domain using normalized form (value range between 0 and 1) and shown as a representative linear profile through the midline of the MC to compare the results with experimentally recorded

diffusion profiles normalized in an equivalent manner (to achieve the value range from 0 to 1). Parameter values used to construct the model and predict diffusion profiles are provided in Table S2.

4.8 Cell Culture

HepG2 Red FLuc (Human hepatoma cell line; purchased at PerkinElmer, referred to as HepG2 in this study) was chosen as the main model cell line based on the perspective aim to easily locate HepG2 cells through the expression of luciferase. This transfected cell line is comparable in cell growth to the parental wild-type HepG2 cell line. The HepG2 cells were cultured using T75 Flask in Dulbecco's Modified Eagle Medium (DMEM, + 4.5 g/L D-Glucose, – Sodium Pyruvate, Gibco) supplemented with 1% streptomycin and penicillin (Biochrom), and 10% fetal bovine serum (Biochrom). They were cultured in a humidified atmosphere composed of 5% CO_2 at 37 °C and passaged at 80%-90% confluence.

Cell density was determined with an automated cell counter (CASY® Model TT from Schärfe System) according to the provided protocol. Each sample was measured in triplicate.

Cells were utilized in passage ranges of P10-25.

4.9 Cell Encapsulation

Cultured HepG2 cells were washed with 5 mL of PBS to remove the remaining medium. 2 mL of Trypsin was added into the T75 Flask and then incubated at 37 °C with 5% CO_2. After 6 min, 8 mL of cell medium was added into the flask to stop trypsinization and resuspend the cells thereby ensuring the separation of cell aggregates. Core fluid solution with resuspended cells (density of 1×10^7 cells·mL^{-1}) was used for encapsulation experiments as inner fluid. The flow rates of inner, middle, and outer fluid were 1 mL·h^{-1}, 1.5 mL·h^{-1}, and 20 mL·h^{-1}, respectively. The generated cell-laden MCs were washed once with cell medium and finally cultured in 24-well culture plate under a humidified atmosphere composed of 5% CO_2 at 37 °C. The culture medium was exchanged with a fresh medium every 2 days.

4.10 Cell Viability and Tumoroid Size Measurements

Cell viability of encapsulated cells was evaluated by using Live/Dead assay (Calcein AM/PI). The cell-laden MCs were first incubated in cell culture medium with 0.016 µg/mL of calcein AM for 45 min. Subsequently, 4 µL of 500 µg/mL PI was added into the cell medium. After 1 min, the stained MCs were observed under the optical microscope (Axio Observer, Zeiss). The green-light detection mode contained a filter set (495 nm beamsplitter, 450-490 nm excitation, and 500-550 nm emission, Zeiss). The red-light detection contained a filter set (570 nm beamsplitter, 538-562 nm excitation, and 570-640 nm emission, Zeiss). The sizes of more than 50 tumoroids in either AL MCs or AL-CS MCs were calculated using ImageJ by measuring the areas of fluorescence from Calcein AM.

4.11 Tumoroid slides and H&E staining

Microcapsules with HepG2 cells were first washed with PBS to remove the cell medium, put into a container, and then fully covered with a solution of 20% sucrose and 7.5% gelatin in PBS. Dry ice was used to cool down the solution and achieve gelation. The solidified gel with microcapsules was stuck on a cutting plate using Tissue Freezing Medium (Leica Microsystem Nussloch), and then cut into 20 µm thick films in a microtome cryostat (CM1850, Leica) at – 35 °C to produce slides. The samples were at first dried at ambient temperature and then fixated for 10 min in acetone. After immersing the samples in warm water for 10 min to dissolve the gelatin, Hematoxylin and Eosin B were used to stain the nucleus (for 3 min) and cytoplasm (for 30 s), respectively. After fixation in a series of ethanol solutions (70%, 85%, 96%, and 100%; for 1 min in each), residual gelatin was washed out by immersing the slides two times for 5 min in Roticlear. Finally, the slides were sealed with RotiMount and coverslips. Subsequent to 24 h of hardening, images were captured under a Axio Imager A1 Microscopy (Zeiss).

4.12 Metabolic Testosterone Assay

HepG2 tumoroids in AL and AL-CS MCs were prepared in advance in a 24 well-plate and cultured at 37 °C under 5% CO_2 for a week with each well containing around 100 capsules. The metabolic activity of encapsulated HepG2 cells was tested upon incubation with testosterone for 4 h.

Testosterone was dissolved in pure ethanol (5 mM) and further diluted in incubation buffer (KHB – Krebs-Henseleit buffer) to reach a concentration of 20 µM. Before the addition of testosterone, encapsulated cells were washed four times with KHB. To do so, a remainder of *ca.* 100-200 µL was left in each well and 800 µL of fresh buffer was added. This reduced the effect on the capsules and limited their disruption. Upon the last washing step, 100-250 µL remained in each cavity and 250 µL of testosterone were added to yield a final incubation concentration of 14-16 µM in a total incubation volume of 500 µL. Testosterone treatment solution, empty AL MCs, and empty AL-CS MCs, were used as controls. After 4 h of incubation at 37 °C under 5% CO_2, 40 µL of the respective incubation solutions were precipitated with acetonitrile (ACN) (160 µL) (1/4, v/v), followed by centrifugation at 4 °C and 18,800 × *g* (14,000 rpm) for 5 min. The resulting supernatant was further diluted with 50% ACN (1/1, v/v) to match the calibrated range of the analytical procedure. The concentration of testosterone and androstenedione was measured using liquid chromatography (LC) in combination with tandem mass spectrometry (MS/MS) in multiple reaction monitoring (MRM) mode as described in the Supporting Information.

Monolayer data was generated in a 96-well plate (0.1-0.3×10^6 cells/well) and 24-well plate (1-4×10^6 cells/well). Cells were therefore seeded the day before the experiment, washed twice with KHB and incubated with 10 µM testosterone in a final volume of 150 µL (96-well plate) and 500 µL (24-well plate) at 37 °C and 5% CO_2. LC-MS/MS analysis was performed as previously described in the Supporting Information.

4.13 Statistical Analysis.

Measured data are reported as mean ± standard deviation (SD) for three independent experiments except where stated otherwise. p-values were calculated using the Student's *t*-test or One-way ANOVA test combined with Tukey's multiple comparison test depending on the number of data groups involved in the comparison. Differences between experimental groups were considered as significant when *$p < 0.05$, **$p < 0.01$, and ***$p < 0.001$, ****$p < 0.0001$, $n \geq 3$.

Supporting Information

Supporting Information is available from the Wiley Online Library or from the author.

Acknowledgements

We would like to thank Aline Morgenegg and Johanna Wodtke for cell culturing experience and instrument training help. We thank Rene Huebner, Ph.D., Rico Illing, PhD., and Bianca Kreisl for capsule sample characterization. We thank Tao Huang, Ph.D., Xinne Zhao, Ph.D., Trang Anh Nguyen Le, and Diana Isabel Sandoval Bojorquez for assistance with microscopy and other experience. We also thank the China Scholarship Council (No. 202006630001) for their support. The partial support by the LiSyM Cancer phase I joint collaborative project DEEP-HCC (Federal Ministry of Education and Research; No. 031L0258B) is also acknowledged.

Received: ((will be filled in by the editorial staff))
Revised: ((will be filled in by the editorial staff))
Published online: ((will be filled in by the editorial staff))

References

[1] R. L. Siegel, K. D. Miller, H. E. Fuchs, A. Jemal, *CA Cancer J. Clin.* **2022**, *72*, 7.

[2] E. R. Shamir, A. J. Ewald, *Nat. Rev. Mol. Cell Biol.* **2014**, *15*, 647.

[3] P. S. Thakuri, C. Liu, G. D. Luker, H. Tavana, *Adv. Healthc. Mater.* **2018**, *7*, e1700980.

[4] A. Doctor, V. Seifert, M. Ullrich, S. Hauser, J. Pietzsch, *Cancers (Basel)* **2020**, *12*.

[5] Y. E. Bar-Ephraim, K. Kretzschmar, H. Clevers, *Nat. Rev. Immunol.* **2020**, *20*, 279.

[6] J. Drost, H. Clevers, *Nat. Rev. Cancer* **2018**, *18*, 407.

[7] H. Wang, D. F. Calvisi, X. Chen, *Semin. Liver Dis.* **2021**, *41*, 19.

[8] H. Xu, X. Lyu, M. Yi, W. Zhao, Y. Song, K. Wu, *J. Hematol. Oncol.* **2018**, *11*, 116.

[9] L. Broutier, G. Mastrogiovanni, M. M. Verstegen, H. E. Francies, L. M. Gavarro, C. R. Bradshaw, G. E. Allen, R. Arnes-Benito, O. Sidorova, M. P. Gaspersz, N. Georgakopoulos, B. K. Koo, S. Dietmann, S. E. Davies, R. K. Praseedom, R. Lieshout, I. J. JNM, S. J. Wigmore, K. Saeb-Parsy, M. J. Garnett, L. J. van der Laan, M. Huch, *Nat. Med.* **2017**, *23*, 1424.

[10] M. Gronholm, M. Feodoroff, G. Antignani, B. Martins, F. Hamdan, V. Cerullo, *Cancer Res.* **2021**, *81*, 3149.

[11] V. Velasco, S. A. Shariati, R. Esfandyarpour, *Microsyst. Nanoeng.* **2020**, *6*, 76.

[12] E. Jabbari, S. K. Sarvestani, L. Daneshian, S. Moeinzadeh, *PLoS One* **2015**, *10*, e0132377.

[13] Z. Gong, L. Huang, X. Tang, K. Chen, Z. Wu, L. Zhang, Y. Sun, Y. Xia, H. Chen, Y. Wei, F. Wang, S. Guo, *Adv. Healthc. Mater.* **2021**, *10*, e2101312.

[14] Z. Luo, X. Zhou, K. Mandal, N. He, W. Wennerberg, M. Qu, X. Jiang, W. Sun, A. Khademhosseini, *Adv. Drug. Deliv. Rev.* **2021**, *176*, 113839.

[15] S. E. Park, A. Georgescu, D. Huh, *Science* **2019**, *364*, 960.

[16] L. Wan, C. A. Neumann, P. R. LeDuc, *Lab Chip* **2020**, *20*, 873.

[17] R. Novak, M. Ingram, S. Marquez, D. Das, A. Delahanty, A. Herland, B. M. Maoz, S. S. F. Jeanty, M. R. Somayaji, M. Burt, E. Calamari, A. Chalkiadaki, A. Cho, Y. Choe, D. B. Chou, M. Cronce, S. Dauth, T. Divic, J. Fernandez-Alcon, T. Ferrante, J. Ferrier, E. A. FitzGerald, R. Fleming, S. Jalili-Firoozinezhad, T. Grevesse, J. A. Goss, T. Hamkins-Indik, O. Henry, C. Hinojosa, T. Huffstater, K. J. Jang, V. Kujala, L. Leng, R. Mannix, Y. Milton, J. Nawroth, B. A. Nestor, C. F. Ng, B. O'Connor, T. E. Park, H. Sanchez, J. Sliz, A. Sontheimer-Phelps, B. Swenor, G. Thompson, 2nd, G. J. Touloumes, Z. Tranchemontagne, N. Wen, M. Yadid, A. Bahinski, G. A. Hamilton, D. Levner, O. Levy, A. Przekwas, R. Prantil-Baun, K. K. Parker, D. E. Ingber, *Nat. Biomed. Eng.* **2020**, *4*, 407.

[18] S. M. Kang, D. Kim, J. H. Lee, S. Takayama, J. Y. Park, *Adv. Healthc. Mater.* **2021**, *10*, e2001284.

[19] L. Shang, Y. Cheng, Y. Zhao, *Chem. Rev.* **2017**, *117*, 7964.

[20] H. Feng, T. Zheng, M. Li, J. Wu, H. Ji, J. Zhang, W. Zhao, J. Guo, *Electrophoresis* **2019**, *40*, 1580.

[21] K. Ren, J. Zhou, H. Wu, *Acc. Chem. Res.* **2013**, *46*, 2396.

[22] Z. Zhu, C. J. Yang, *Acc. Chem. Res.* **2017**, *50*, 22.

[23] T. Schneider, J. Kreutz, D. T. Chiu, *Anal. Chem.* **2013**, *85*, 3476.

[24] R. Song, M. S. Abbasi, J. Lee, *Microfluid. Nanofluid.* **2019**, *23*.

[25] S. H. Kim, D. A. Weitz, *Angew. Chem. Int. Ed. Engl.* **2011**, *50*, 8731.

[26] P. Zhu, L. Wang, *Lab Chip* **2016**, *17*, 34.

[27] P. Dimitriou, J. Li, G. Tornillo, T. McCloy, D. Barrow, *Glob. Chall.* **2021**, *5*, 2000123.

[28] Y. Ding, P. D. Howes, A. J. deMello, *Anal. Chem.* **2020**, *92*, 132.

[29] K. Matula, F. Rivello, W. T. S. Huck, *Adv. Biosyst.* **2020**, *4*, e1900188.

[30] D. G. Alonso, M. C. Yu, H. J. Qu, L. Ma, F. Shen, *Adv. Biosyst.* **2019**, *3*.

[31] N. Wen, Z. Zhao, B. Fan, D. Chen, D. Men, J. Wang, J. Chen, *Molecules* **2016**, *21*.

[32] Y. Wang, H. Liu, M. Zhang, H. Wang, W. Chen, J. Qin, *Biomater. Sci.* **2020**, *8*, 5476.

[33] C. X. Zhao, D. Chen, Y. Hui, D. A. Weitz, A. P. J. Middelberg, *Chemphyschem* **2017**, *18*, 1393.

[34] Y. Zhu, L. Sun, X. Fu, J. Liu, Z. Liang, H. Tan, W. Li, Y. Zhao, *Chem. Eng. J.* **2021**, *424*.

[35] H. Liu, Y. Wang, H. Wang, M. Zhao, T. Tao, X. Zhang, J. Qin, *Adv. Sci. (Weinh)* **2020**, *7*, 1903739.

[36] C.-X. Xie, T.-C. Tian, S.-T. Yu, L. Li, *J. Appl. Polym. Sci.* **2019**, *136*.

[37] K. Y. Lee, D. J. Mooney, *Prog. Polym. Sci.* **2012**, *37*, 106.

[38] F. Shao, L. Yu, Y. Zhang, C. An, H. Zhang, Y. Zhang, Y. Xiong, H. Wang, *Front. Bioeng. Biotechnol.* **2020**, *8*, 583065.

[39] S. Utech, R. Prodanovic, A. S. Mao, R. Ostafe, D. J. Mooney, D. A. Weitz, *Adv. Healthc. Mater.* **2015**, *4*, 1628.

[40] W.-H. Tan, S. Takeuchi, *Adv. Mater.* **2007**, *19*, 2696.

[41] G. Fang, H. Lu, L. Rodriguez de la Fuente, A. M. K. Law, G. Lin, D. Jin, D. Gallego-Ortega, *Adv. Sci. (Weinh)* **2021**, *8*, e2102418.

[42] A. Ashimova, S. Yegorov, B. Negmetzhanov, G. Hortelano, *Front. Bioeng. Biotechnol.* **2019**, *7*, 380.

[43] F. He, T. Tao, H. Liu, Y. Wang, K. Cui, Y. Guo, J. Qin, *ACS Appl. Bio Mater.* **2021**, *4*, 1584.

[44] K. Alessandri, B. R. Sarangi, V. V. Gurchenkov, B. Sinha, T. R. Kiessling, L. Fetler, F. Rico, S. Scheuring, C. Lamaze, A. Simon, S. Geraldo, D. Vignjevic, H. Domejean, L. Rolland, A. Funfak, J. Bibette, N. Bremond, P. Nassoy, *Proc. Natl. Acad. Sci. U S A* **2013**, *110*, 14843.

[45] H. Wang, H. Liu, X. Zhang, Y. Wang, M. Zhao, W. Chen, J. Qin, *ACS Appl. Mater. Interfaces* **2021**, *13*, 3199.

[46] H. Liu, Y. Wang, Y. Yu, W. Chen, L. Jiang, J. Qin, *J. Biomed. Mater. Res. B Appl. Biomater.* **2019**, *107*, 2527.

[47] Z. Nie, M. Seo, S. Xu, P. C. Lewis, M. Mok, E. Kumacheva, G. M. Whitesides, P. Garstecki, H. A. Stone, *Microfluid. Nanofluid.* **2008**, *5*, 585.

[48] N. Cao, X. B. Chen, D. J. Schreyer, *ISRN Chem. Eng.* **2012**, *2012*, 1.

[49] G. Lawrie, I. Keen, B.Drew, A. Chandler-Temple, L. Rintoul, P. Fredericks, L. Grøndahl, *Biomacromolecules* **2007**, *8*, 2533.

[50] A. Pawlak, M. Mucha, *Thermochim. Acta* **2003**, *396*, 153.

[51] D. Sun, Y. Liu, H. Wu, Y. Ren, X. Ma, H. Wu, G. Sun, *Biotechnol. Appl. Biochem.* **2018**, *65*, 263.

[52] Z. Petrasek, P. Schwille, *Biophys. J.* **2008**, *94*, 1437.

[53] J. V. Silva, P. D. Peixoto, S. Lortal, J. Floury, *J. Dairy Sci.* **2013**, *96*, 6186.

[54] Merck, FITC-labelled polysaccharides, https://www.sigmaaldrich.com/DE/en/technical-documents/technical-article/cell-cultureand-cell-culture-analysis/imaging-analysis-and-live-cell-imaging/fluorescently-labeleddextrane#1, accessed: **2022**.

[55] R. H. Li, D. H. Altreuter, F. T. Gentile, *Biotechnol. Bioeng.* **1995**, *50*, 365.

[56] J. M. Llovet, R. K. Kelley, A. Villanueva, A. G. Singal, E. Pikarsky, S. Roayaie, R. Lencioni, K. Koike, J. Zucman-Rossi, R. S. Finn, *Nat. Rev. Dis. Primers* **2021**, *7*, 6.

[57] S. Lemm, S. Köhler, R. Wodtke, F. Jung, J. Küpper, J. Pietzsch, M. Laube, *Nuclear Medicine and Biology* **2022**, *108-109*, S66.

[58] A. Piotrowska, J. Wierzbicka, A. Rybarczyk, R. C. Tuckey, A. T. Slominski, M. A. Zmijewski, *Int. J. Oncol.* **2019**, *54*, 1481.

[59] C. A. Schneider, W. S. Rasband, K. W. Eliceiri, *Nat. Methods* **2012**, *9*, 671.

[60] A. Fick, Diffusion Equation_Fick's Laws of Diffusion, https://www.comsol.de/multiphysics/diffusion-equation?parent=diffusion-0402-392-412, accessed: January, **2015**.